Enhanced-Resolution SMAP Brightness Temperature Image Products

David G. Long, *Fellow, IEEE*, Mary J. Brodzik, *Member, IEEE*, and Molly A. Hardman

***Abstract*— The NASA-sponsored Calibrated Passive Microwave Daily Equal-Area Scalable Earth Grid 2.0 Brightness Temperature (CETB) Earth System Data Record Project team has generated a multisensor, multidecadal time series of high-resolution radiometer products designed to support climate studies. This project uses image reconstruction techniques to generate conventional and enhanced-resolution daily brightness temperature images on a standard set of map projections. Sensors included in CETB are the Aqua Advanced Microwave Scanning Radiometer–Earth Observing System (AMSR-E), Scanning Multichannel Microwave Radiometer, and all Special Sensor Microwave/Imager and Special Sensor Microwave Imager/Sounder radiometers. These span frequencies between 6 and 89 GHz. This paper considers the issues of adding the L-band (1.6 GHz) Soil Moisture Active Passive (SMAP) radiometer measurements to the CETB climate record, with emphasis on optimizing the reconstruction to provide the highest possible spatial resolution at the lowest noise level. SMAP radiometer reconstruction on SMAP-standard grids is also considered. Simulation is used to optimize the reconstruction, and the results confirmed using actual data. A comparison of the performance of the Backus–Gilbert approach and the radiometer form of the Scatterometer Image Reconstruction algorithm is provided. These are compared to the conventional drop-in-the-bucket gridded imaging.**

***Index Terms*— Brightness temperature, Calibrated Passive Microwave Daily Equal-Area Scalable Earth Grid 2.0 Brightness Temperature (CETB), radiometer, reconstruction, Soil Moisture Active Passive (SMAP).**

I. Introduction

EXPLOITING the availability of new fundamental climate data records for passive microwave observations of Earth, the NASA Making Earth Science Data Records for Use in Research Environments Calibrated Passive Microwave Daily Equal-Area Scalable Earth (EASE)-Grid 2.0 Brightness Temperature ESDR (CETB) Earth System Data Record (ESDR) Project team has created a single, consistently processed, multisensor ESDR of Earth-gridded microwave brightness temperature (T_B) images spanning from 1978 to the present [1]. The CETB ESDR includes data from the Nimbus-7 Scanning Multichannel Microwave Radiometer (SMMR), the Special Sensor Microwave/Imager (SSM/I) and Special Sensor Microwave Imager/Sounder (SSMIS) series sensors, and the Aqua Advanced Microwave Scanning Radiometer–Earth Observing System (AMSR-E). The CETB generates both conventional and enhanced-resolution T_B images on standard map projections [2]. Designed to serve the land surface and polar snow/ice communities, the new products are intended to replace existing heritage gridded satellite passive microwave products with a single, consistently processed ESDR [1]. Although there are variations between sensors, this data record is an invaluable asset for studies of climate and climate change.

Soil Moisture Active Passive (SMAP) radiometer data offer an important addition to the CETB data set. To this end, this paper considers the application of the CETB-developed enhanced-resolution processing to SMAP radiometer data to augment the existing CETB ESDR. The processing algorithm parameters are optimized for use with SMAP, and a performance comparison between reconstruction with the radiometer form of the Scatterometer Image Reconstruction algorithm (rSIR) and the Backus–Gilbert (BG) approach is provided.

A key part of the sensor T_B processing is the conversion of the swath-based measurements to the Level 3 Earth-centered grid. Algorithms to transform radiometer data from swath to gridded format are characterized by a tradeoff between noise and spatial and temporal resolution. Conventional drop-in-the-bucket (DIB), also known as gridding or GRD, techniques provide low-noise, low-resolution products, but higher resolution (with potentially higher noise) products are possible using image reconstruction techniques. By including products with both processing options in the CETB, users can compare and choose which option better suits their particular research application. This paper presents simulation results that are used to select the nominal pixel size for enhanced-resolution processing for SMAP, the number of iterations used in rSIR, and the optimum γ parameter employed in BG.

This paper focuses on the production of Earth-center T_B image products. From these, soil moisture can be derived. Multiple SMAP radiometer products are planned: conventional and enhanced-resolution multipass images on both CETB-compatible 25 km and finer grids, as well as SMAP-standard 36 km and finer grids.

This paper is organized as follows. After some brief background in Section II, a review of the theory of radiometer image reconstruction is provided in Section III. Section IV employs simulation to select the optimum parameters for image formation for SMAP radiometer data. The pixel spatial response function (SRF) is computed in Section V. Actual data

Manuscript received October 27, 2018; revised December 10, 2018; accepted December 20, 2018. Date of publication January 31, 2019; date of current version June 24, 2019. This work was supported in part by NASA under Grant NNX16AN01G. *(Corresponding author: David G. Long.)*

D. G. Long is with the Department of Electrical and Computer Engineering, Brigham Young University, Provo, UT 84602 USA (e-mail: long@ee.byu.edu).

M. J. Brodzik and M. A. Hardman are with the National Snow & Ice Data Center, Cooperative Institute for Research in Environmental Sciences, University of Colorado Boulder, Boulder, CO 80303 USA.

Color versions of one or more of the figures in this paper are available online at http://ieeexplore.ieee.org.

Digital Object Identifier 10.1109/TGRS.2018.2889427

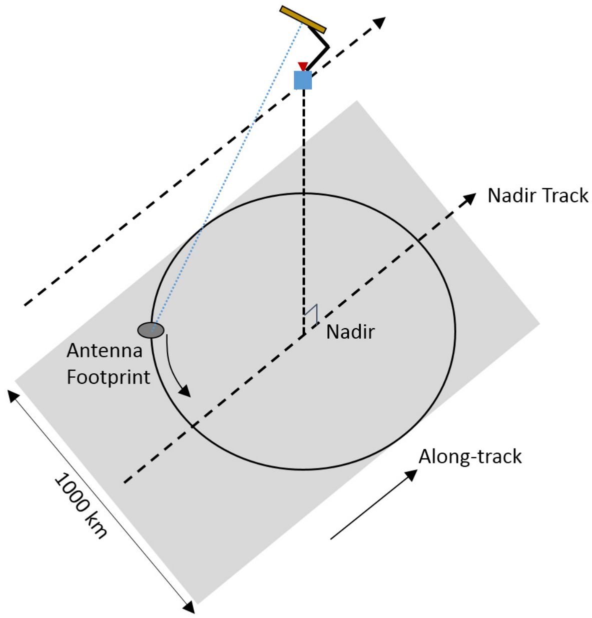

Fig. 1. Illustration of the SMAP radiometer swath. The antenna and feed are spun about the vertical axis. The incidence angle is essentially constant as the antenna scans the surface. (Not to scale.)

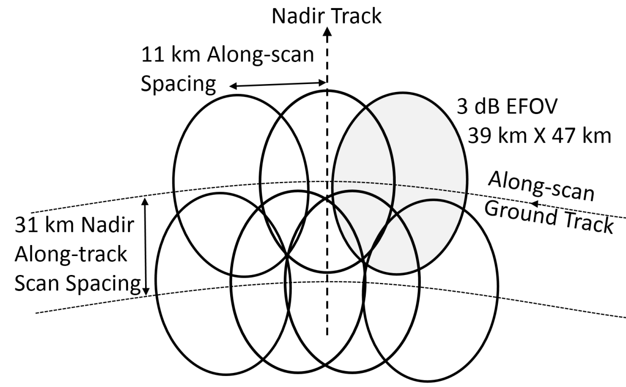

Fig. 2. Illustration of the individual 3-dB antenna footprints for several measurements for two consecutive rotations of the antenna. The rotations are spaced approximately 31 km apart in the along-track direction, while the antenna instantaneous effective field of view for individual measurements are spaced about 11 km apart in the along-scan direction. (Not to scale).

results are provided in Section VI, followed by a summary conclusion in Section VII.

II. Background

The SMAP sensor includes both active and passive channels; however, due to the early failure of the active channels, only the passive radiometer channels are considered in this paper. Operating at L-band (1.41 GHz) with a 24-MHz bandwidth, the SMAP radiometer collects measurements of the horizontal (H), vertical (V), and third and fourth Stokes parameter polarizations with a total radiometric uncertainty of 1.3 K [3]. The SMAP spacecraft was launched in January 2015 and flies in a 685-km altitude, 98.1° inclination polar orbit.

The SMAP swath and scanning concept are illustrated in Fig. 1. The antenna spin rate is 14.6 rpm which, when coupled with the along-track motion of the spacecraft, produces a helical scan pattern on the surface with an along-track spacing of approximately 31 km between antenna rotations. The V, H, and third and fourth Stokes parameter brightness temperature measurements are collected at a nominal incidence angle of approximately 53°. The polarizations share the same physical aperture and so their antenna footprints are collocated [3]. A zoomed-in view of the arrangement of the antenna footprints on the surface for consecutive measurements of two rotations is shown in Fig. 2.

A. CETB T_B Image Products

All algorithms to transform radiometer data from swath to gridded format are characterized by a tradeoff between noise and spatial resolution [2], [9], [10]. In generating gridded data, when multiple measurements are combined, the resulting images represent an average of the measurements over the averaging period. The CETB product includes both low-noise (low-resolution) gridded data and enhanced-resolution data grids (which can have potentially higher noise), to enable product users to compare and choose which option better suits a particular research application. The products are created on compatible (nested) grids using a standard EASE-Grid 2.0 map projection [4], [5]. This is the same map projection employed by the SMAP project [3], although the pixel sizes differ between the SMAP and CETB products. The CETB provides T_B Northern Hemisphere (E2N), Southern Hemisphere (E2S), and Tropical/Temperate (E2T) images using DIB at 25 km and rSIR at up to 3.125 km on the nested EASE2-grids [1].

In the conventional-resolution CETB product, the individual radiometer channels are separately gridded to a single coarse-resolution grid using DIB gridding. For the DIB gridding algorithm, the key information required is the location of the measurement. The center of each measurement location is mapped to an output projected grid cell or pixel. All measurements within the specified time period whose center locations fall within the bounds of a particular grid cell are averaged together. The unweighted average becomes the reported pixel T_B value for that grid cell.

The effective spatial resolution of the DIB product is defined by a combination of the pixel size and spatial extent of the 3-dB antenna footprint size [9] and has the advantage of not requiring any information about the antenna pattern [2]. Since the measurement footprints can extend outside of the pixel, the effective resolution is coarser than the pixel size. Although the pixel size can be arbitrarily set, the effective resolution is, to first order, the sum of the pixel size plus the larger footprint dimension [2].

Finer spatial resolution CETB products are generated using reconstruction, primarily with the rSIR algorithm, which provides results similar to the BG approach and requires less computation [2]. Both BG and rSIR use regularization to tradeoff noise and resolution. However, BG is based on least squares and depends on a subjectively chosen tradeoff parameter for regularization; rSIR employs maximum entropy reconstruction with regularization accomplished by limiting the number of iterations and thereby only producing partial reconstruction.

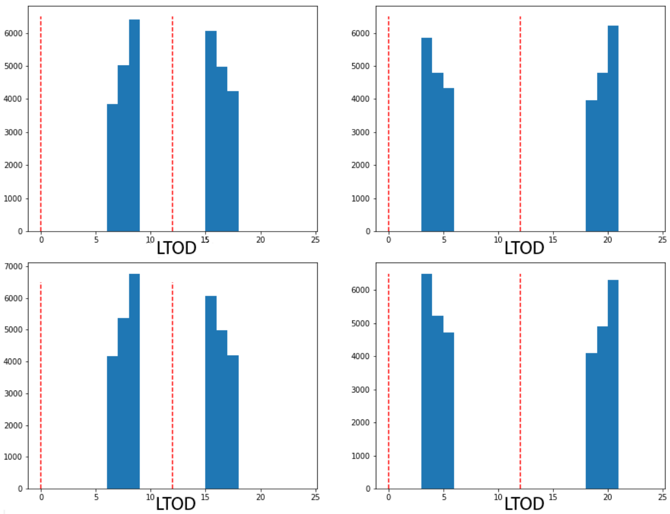

Fig. 3. Histograms of the measurement ltod for SMAP radiometer measurements falling within a 1° latitude band at (Top) 70°–71° N and (Bottom) 70°–71° S for July 3, 2015. Other days are similar. Note that all the measurements fall into only one of two narrow ltod time periods centered at approximately 08:00 and 16:00 h in the Northern Hemisphere (left) and 04:00 and 20:00 h in the Southern Hemisphere (right). Although the center varies with latitude, any point on Earth is observed at one of two times within ±90 min.

B. Local-Time-of-Day

To produce twice-daily images, CETB products combine data from multiple passes based on the measurements' local-time-of-day (ltod). Only measurements with a similar ltod are combined. This minimizes the fluctuations in the observed T_B at high latitudes due to changes in physical temperature from daily temperature cycling. Two images per day are produced, separated by 12 h (morning and evening), with improved temporal resolution, permitting resolution of diurnal variations [2].

The observed microwave brightness temperature is the product of surface physical temperature and surface emissivity. As a result of the orbit geometry, the ltod of sun-synchronous radiometer observations at a given location on the earth falls within two narrow time windows. At the equator, these correspond to the ascending and descending orbit passes. Near the poles, the windows widen to several hours but remain relatively narrow. Since surface temperatures can fluctuate widely during the day, daily averaging is not generally useful since it smears diurnal temperature fluctuations in the averaged T_B. However, it is reasonable to split the data into two distinct ltod images per day [2]. The CETB adopts the ltod division scheme for the northern and southern hemisphere. At low latitudes, which typically have few overlapping swaths at similar ltod in the same day, ltod division is equivalent to ascending/descending division. An ancillary image is included for each sensor in the CETB to describe the effective time average of the measurements combined into the pixel for a particular day. This enables the investigators to explicitly account for the ltod temporal variation of the measurements included in a particular pixel.

This same approach is used for SMAP radiometer observations. Histograms of the ltod SMAP radiometer measurements falling within two narrow high-latitude bands (70°–71° N and S) are shown in Fig. 3. Note that a natural division in the measurement ltod is at 00:00 and 12:00 h. Following [1], [2], when processing SMAP radiometer data, the CETB creates two separate ltod images per day using these temporal divisions.

C. Radiometer Spatial Response Function

The effective spatial resolution of the image products is determined by the spatial measurement response function (MRF) of the sensor and by the image formation algorithm used. The MRF is determined by the antenna gain pattern, the scan geometry (notably the antenna scan angle), and the measurement integration period. The MRF for a general microwave radiometer is derived in [2]. This section provides a brief summary of the derivation of the MRF and the algorithms used for T_B image construction from the measurements. We note that for T_B image reconstruction, the MRF can be treated as zero everywhere but in the direction of the surface.

Microwave radiometers measure the thermal emission, sometimes called the Plank radiation, radiating from natural objects [11]. In a typical radiometer, an antenna is scanned over the scene of interest and the output power from the carefully calibrated receiver is measured as a function of scan position. The reported signal is a temporal average of the filtered received signal power. The observed power is related to receiver gain and noise figure, antenna loss, physical temperature of the antenna, antenna pattern, and scene brightness temperature [11].

Because the antenna is rotating during the integration period, the *effective* antenna gain pattern G_s is a smeared version of the instantaneous antenna pattern G, that is,

$$G_s(\theta, \phi) = T_p^{-1} \int_0^{T_p} G(\theta, \phi + \omega_r t) dt \tag{1}$$

where T_p is the integration period and ω_r is the antenna rotation rate. In simplified form, the observed brightness temperature measurement z can be expressed as

$$z = \iint \mathrm{MRF}(x, y) T_B(x, y) dx dy + T_{\mathrm{non}} \tag{2}$$

where T_{non} is the effective brightness temperature contribution of sources not related to the surface brightness temperature distribution $T_B(x, y)$. MRF(x, y) is the MRF expressed in surface coordinates x and y

$$\mathrm{MRF}(x, y) = G_b^{-1} G_s(x, y) \tag{3}$$

where G_b is the spatially integrated gain over the surface

$$G_b = \iint G_s(x, y) dx dy. \tag{4}$$

Careful calibration and preprocessing estimates and removes T_{non} from the measurements. The image formation estimates the surface brightness temperature map $T_B(x, y)$ from the calibrated measurements z.

III. Gridding and Reconstruction

Algorithms that generate 2-D gridded images from raw measurements are characterized by a tradeoff between noise and spatial resolution. Our goal is to estimate an image of

TABLE I
SMAP NESTED GRID RESOLUTIONS

Grid Resolution
36 km*
9 km
6 km†
3 km

* Base pixel size.
† Non-standard SMAP grid size.

TABLE II
CETB NESTED GRID RESOLUTIONS

Grid Scale Factor	Grid Resolution
$1 = 2^0$	25 km*
$2 = 2^1$	12.5 km
$4 = 2^2$	6.25 km
$8 = 2^3$	3.125 km
$16 = 2^4$	1.5625 km

* Base pixel size.

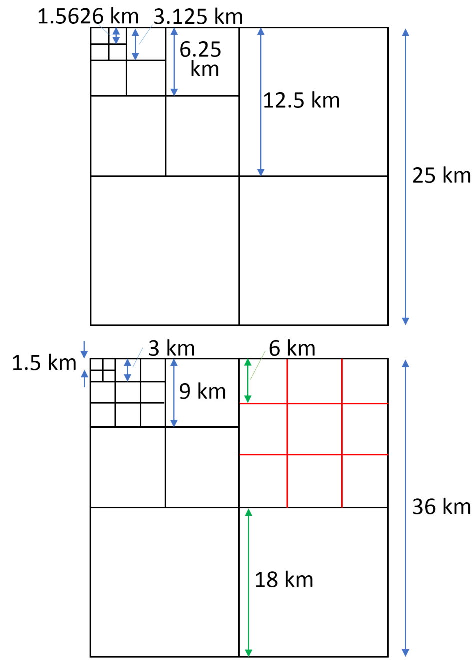

Fig. 4. Nesting configuration of the (Left) CETB and (Right) SMAP project grids. The 6-km nested SMAP grid is an extension of the SMAP standard.

the surface $T_B(x, y)$ from the sensor T_B measurements. The "nominal" resolution of the T_B measurements is typically considered to be the size of the 3-dB response pattern of the MRF. Although the effective resolution of DIB imaging is no finer than the effective resolution of the measurements, reconstruction techniques can yield higher effective resolution if spatial sampling requirements are met.

As previously noted, the CETB team generated both low-noise gridded data and enhanced-resolution data products [1]. The low resolution gridded data use the DIB method described below. These products are termed "low resolution" or "nonenhanced resolution" and denoted as gridded (GRD or DIB) products. Higher resolution products are generated using one of two image reconstruction methods: the rSIR algorithm or the BG image formation method, as described below. The CETB independently optimizes the resolution for each channel in the high-resolution products. The product is Earth-located (in contrast to swath-based) using the EASE-Grid 2.0 [4], [5] map projection.

In generating CETB gridded data, only the measurements from a single sensor and channel are processed. Measurements combined into a single grid element may have different incidence angles (though the incidence angle variation is small) and azimuth angles relative to north. Measurements from multiple orbit passes over a narrow local time window may be combined. When multiple measurements are combined, the resulting images represent a temporal average of the measurements over the averaging period. There is an implicit assumption that the surface characteristics remain constant over the imaging period and that there is no azimuth variation in the true surface T_B. For both conventional-resolution (nonenhanced) and enhanced-resolution images, the effective gridded image resolution depends on the number of measurements and the precise details of their overlap, orientation, and spatial locations.

Two image grids are considered: SMAP-compatible and CETB-compatible. Both use the EASE-Grid 2.0 projection [4], [5], but at different resolutions, see Tables I and II. In the CETB, radiometer channels are gridded at enhanced resolution on nested grids at power of 2 relationships to the base 25-km grid, see Table II and Fig. 4. This embedded gridding simplifies overlaying grids from different resolutions. For SMAP, a slightly different scheme is employed based on a base 36-km grid as shown in Table I and Fig. 4.

A. Reconstruction Algorithms

In the reconstruction algorithms, the MRF for each measurement is used in estimating the surface T_B on a fine-scale grid. As previously noted, the MRF is determined by the antenna gain pattern, the scan angle geometry, and the measurement integration period. The MRF describes how much the emissions from a particular location on the surface contribute to the observed T_B value.

For image formation, T_B is computed at each pixel on the EASE-Grid 2.0 grid. If the measurement sampling pattern were uniform on this grid, classic reconstruction and deconvolution techniques could be used. However, the sensor measurements are not aligned with the Earth-centered grid, which results in an irregular sampling pattern. Thus, signal reconstruction based on irregular sampling is applied to the problem. Since the signal measurements are noisy, rather than do full signal reconstruction, which could produce excessive noise enhancement, only partial reconstruction is computed. This is done by regularization, which imposes a smoothing constraint on the reconstructed image and preventing extreme values.

The rSIR has proven effective in generating high-resolution brightness temperature images [2], [9]. The rSIR estimate approximates a maximum-entropy solution to an underdetermined equation and least-squares to an overdetermined system. rSIR provides results superior to the Backus–Gilbert method, and with significantly less computation [2].

Regularization is built into BG and rSIR to enable a tradeoff between signal reconstruction accuracy and noise enhancement. Both approaches enable estimation of the surface brightness on a finer grid than is possible with the conventional DIB approaches, i.e., the resulting brightness temperature estimate has a finer effective spatial resolution than DIB methods. As a result, the results are often called "enhanced resolution," though, in fact, the reconstruction algorithm merely exploits the available information to reconstruct the original signal at higher resolution than DIB gridding, based on the assumption of a bandlimited signal [10]. The potential resolution enhancement depends on the sampling density and the MRF; however, improvements of 25%–1000% in the effective resolution have been demonstrated in practice for particular applications. For radiometer enhancement, the effective improvement in resolution tends to be limited, and, in practice, is typically less than 100%. Nevertheless, the resulting images have improved spatial resolution and information. Note that in order to meet Nyquist requirements for the signal processing, the pixel resolution of the images must be finer than the effective resolution by at least a factor of 2. When multiple passes over the area are combined, reconstruction algorithms intrinsically exploit the resulting oversampling of the surface to improve the effective spatial resolution in the final image.

For comparison, note that the effective resolution for DIB gridding is essentially the sum of pixel grid size plus the spatial dimension of the measurement, which is typically defined by the half-power or the 3-dB beamwidth. Based on Nyquist considerations, the highest representable spatial frequency for DIB gridding is twice the grid spacing.

B. rSIR Reconstruction

Noting that others (e.g., [12]) are pursuing the use of BG for SMAP processing, our emphasis in this paper is on the use of rSIR. However, it is useful to compare rSIR and BG performance, which also provides insight into the reconstruction performance of both algorithms.

In the reconstruction the surface brightness temperature distribution $T_B(x, y)$ is treated as a discrete signal sampled at the map pixel spacing and is estimated from the noisy measurements z. To summarize the reconstruction approach, T_B is vectorized over an $N_x \times N_y$ pixel grid into a single dimensional variable $a_j = T_B(x_j, y_j)$, where $j = l + N_x k$. A particular calibration-corrected measurement x_i can be expressed as

$$z_i = \sum_{j \in \text{ image}} h_{ij} a_j \tag{5}$$

where $h_{ij} = \text{MRF}(x_l, y_k)$ is the discretely sampled MRF for the ith measurement evaluated at the jth pixel center. The MRF is typically negligible some distance from the measurement, so the sum need only be computed over an area local to the measurement position. The h_{ij} are normalized so that $\sum_j h_{ij} = 1$. Written as a matrix equation for the collection of available measurements, (5) becomes

$$\vec{T} = \mathbf{H}\vec{a} \tag{6}$$

where $\mathbf{H}$ contains the sampled MRF for each measurement and $\vec{T}$ and $\vec{a}$ are vectors composed of the measurements z_i and the sampled surface brightness temperature a_j, respectively. The matrix $\mathbf{H}$ is sparse, and may be overdetermined or underdetermined depending on the sampling density.

The rSIR algorithm iteratively solves (6) [9]. It approximates a maximum-entropy solution to an underdetermined equation and a least-squares solution to an overdetermined system. The first iteration of rSIR, termed "AVE" (for weighted AVErage), is a simple estimate of T_B with the jth pixel given by

$$a_j^0 = \frac{\sum_i h_{ij} z_i}{\sum_i h_{ij}}. \tag{7}$$

At the kth ($k > 0$) iteration of rSIR, the jth image pixel a_j^k is computed using

$$\begin{aligned}
f_i^k &= \frac{\sum_n h_{in} a_n^k}{\sum_n h_{in}} \\
d_i^k &= \sqrt{z_i / f_i^k} \\
u_{i,j}^k &= \begin{cases} \left[\dfrac{1}{2 f_i^k} \left(1 - \dfrac{1}{d_i^k} \right) + \dfrac{1}{a_j^k d_i^k} \right]^{-1}, & d_k^k \geq 1 \\ \left[\dfrac{1}{2} f_i^k \left(1 - d_i^k \right) + a_j^k d_i^k \right], & d_k^k < 1 \end{cases} \\
a_j^{k+1} &= \frac{\sum_i h_{ij} u_{i,j}^k}{\sum_i h_{ij}}.
\end{aligned}$$

The more general BG inversion method [6], [7] was first applied to radiometer data by Stogryn [8] and then by others [2], [9], [20], [21] to improve the spatial resolution of surface brightness temperature fields. In a discrete implementation of BG, the T_B estimate $\widehat{a_j}$ of the jth pixel is written as

$$\widehat{a_j} = \sum_{i \in \text{ nearby}} w_{ij} z_i \tag{8}$$

where the sum is computed over nearby pixels and where w_{ij} are weights selected so that $\sum_i w_{ij} = 1$. To generate a unique solution for a particular pixel j, the squared signal error term Q_R is expressed as

$$Q_R = \left(\sum_{j \in \text{ nearby}} w_{ij} h_{ij} - 1 \right)^2 \tag{9}$$

and the noise error term Q_N written as

$$Q_N = \vec{w}^T \mathbf{E} \vec{w} \tag{10}$$

where $\mathbf{E}$ is the noise covariance matrix. The total error Q is

$$Q = Q_R \cos\gamma + \omega Q_N \sin\gamma \tag{11}$$

where ω is an arbitrary dimensional tuning parameter and γ is a subjectively selected parameter to tradeoff noise and signal error. For SMAP, the matrix $\mathbf{E}$ is a diagonal matrix with diagonal entries $\Delta T/2$ where ΔT is the radiometer channel noise standard deviation. Varying γ alters the solution for the weights between a least-squares solution and a minimum noise solution.

The total error Q is minimized when the weight vector for the pixel is selected as [7]

$$\vec{w} = \mathbf{Z}^{-1}\left(v_i \cos\gamma + \frac{1 - \vec{u}^T\mathbf{Z}^{-1}\vec{u}\cos\gamma}{\vec{u}^T\mathbf{Z}^{-1}\vec{u}}\right) \tag{12}$$

where

$$\vec{u}_i = \sum_j h_{ij} = \vec{v}_i$$
$$\mathbf{Z} = \mathbf{G}_j \cos\gamma + \omega\mathbf{E}\sin\gamma$$
$$\mathbf{G}_j = h_{ij}h_{kj}.$$

For both rSIR and BG, we follow [2] to define "nearby" as regions where the MRF is within 8 dB of the peak response, which helps minimize computation. Outside this region, the MRF is treated as zero. TB is separately calculated for each output pixel and each channel using the particular measurement geometry antenna pattern at the swath location and Earth azimuth scan angle. This increases the computational load but results in the best quality images. Due to occasional poor matrix condition numbers, the BG method occasionally produces artifacts. These are eliminated with the aid of a median-threshold filter [2].

Note that in applying both DIB and reconstruction processing to SMAP, each polarization channel is separately and independently computed. No power normalization is applied.

IV. Performance Simulation

To compare the performance of the reconstruction techniques, it is helpful to use simulation. The results of these simulations inform the tradeoffs needed to select processing algorithm parameters. A simplified, but still realistic, simulation of the SMAP geometry and SRF is used to generate simulated measurements of a synthetic Earth-centered image. From both noisy and noise-free measurements, DIB, AVE, rSIR, and BG images are created, with error (mean, and root-mean-square [rms]) determined for each case. This is repeated separately for each channel. The measurements are assumed to have a standard deviation of $\Delta T = 1$ K. The results are relatively insensitive to the ΔT value used. The same simulated measurements are used for both BG and rSIR.

Following [2], two different pass cases are considered: the single-pass case and the case with two overlapping passes. The simulation shows that the relative performance of rSIR and BG are the same for both cases, so we show only one case in this paper. Since multiple passes are often combined, the two-pass case is emphasized in the simulations presented.

An arbitrary "truth" image is generated with representative features including spots of varying sizes, edges, and areas of constant and gradient T_B, see Fig. 5. Based on the SMAP measurement geometry, simulated locations of antenna boresite at the center of the integration period are plotted in Fig. 6 for both a single pass and two passes.

An analysis of the rSIR reconstruction accuracy relative to the accuracy of the MRF was conducted by [2]. They found that because rSIR does only partial reconstruction, it is tolerant to errors in describing the MRF. Hence, a simplified model for the MRF can be used. The SMAP MRF is modeled with a

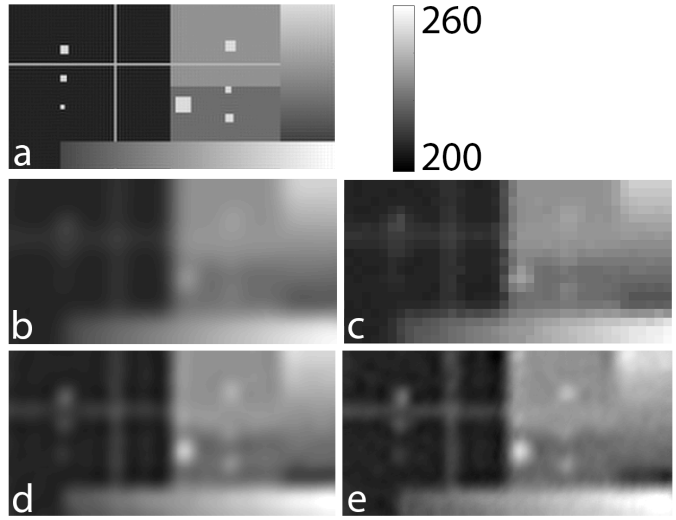

Fig. 5. T_B images from different methods. (a) True image used in simulation. The true image has been bandpass filtered to 10-km effective resolution, which accounts for the Gibbs phenomena at region boundaries. (b) AVE (first iteration of rSIR). (c) DIB (25 km). (d) rSIR 20 iterations. (e) BG with $\gamma = 0.425\pi$. Error statistics are summarized in Table III.

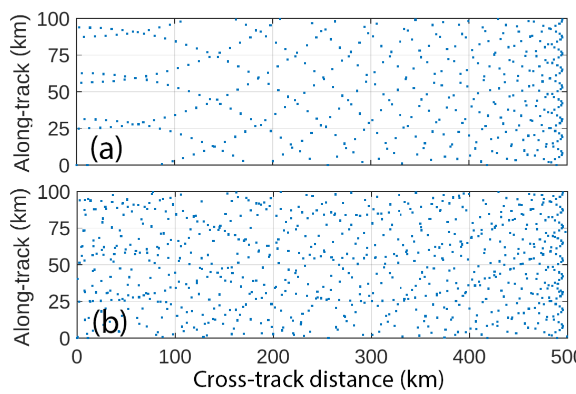

Fig. 6. Illustrations of the measurement locations within a small area of the SMAP coverage swath. (a) Locations for a single orbit pass. (b) Locations for two passes. In this case, the along-track/cross-track grid shown is for the first pass only. The second pass has a different alignment.

2-D Gaussian function whose 3-dB (half-power) point matches the footprint size. The orientation of the ellipse varies over the swath according to the azimuth antenna angle. To apply the MRF in the processing, the MRF is positioned at the center of the nearest neighbor pixel to the measurement location and oriented with the azimuth antenna angle. The values of the discrete MRF are computed at the center of each pixel in a box surrounding the pixel center. The size of the box is defined to be the smallest enclosing box for which the sampled antenna pattern is larger than a minimum gain threshold of -30 dB relative to the peak gain. A second threshold (typically -8 dB) defines the gain cutoff used in the rSIR and BG processing. The latter threshold defines the N_{size} parameter used by Long and Daum [9] and is the same value used in the CETB for other satellite radiometers.

The image pixel size defines how well the MRF can be represented in the reconstruction processing and the simulation. A representative plot of the MRF sampling for each channel for each pixel size under consideration is shown

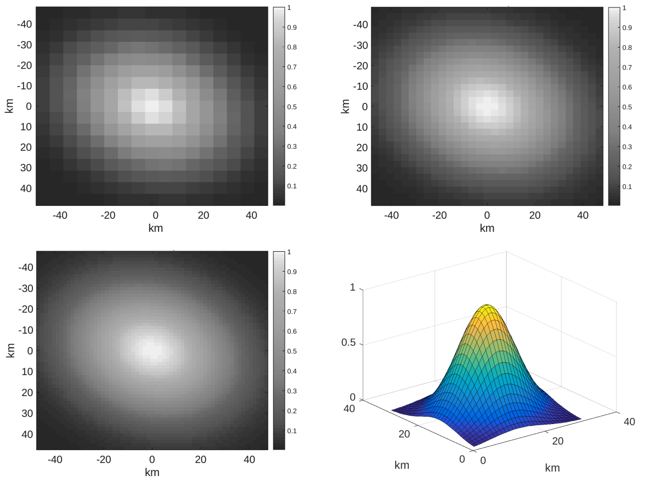

Fig. 7. Illustration of a particular sampled MRF for different pixel sizes. (Top left) 6.25-km pixels. (Top right) 3.125-km pixels. (Bottom left) 1.5625-km pixels. (Bottom right) Perspective view of the 3.125-km case.

TABLE III

ERROR STATISTICS FOR ONE- AND TWO-PASS SIMULATIONS ON A CETB 3.125-km GRID. rSIR USES 30 ITERATIONS. BG USES $\gamma = 0.425\pi$

Case	Passes	Mean	STD	RMS
DIB	1	-0.19	6.10	6.10
AVE	1	0.00	6.20	6.20
BG	1	-0.48	5.61	5.63
rSIR	1	0.02	5.12	5.12
DIB	2	-0.22	6.13	6.13
AVE	2	-0.02	6.08	6.08
BG	2	-0.27	5.28	5.28
rSIR	2	0.01	5.16	5.16

in Fig. 7. Note that as the pixel size is decreased, the sampled MRF more closely resembles the continuous MRF, thereby reducing quantization error; however, reducing the pixel size increases the computation and size of the output products. Finer resolution leads to less "chunky" appearing images on a finer posting grid. Note that the image results need to be posted at twice the highest frequency to meet Nyquist requirements.

Separate images are created for both noisy and noise-free measurements. Error statistics (mean, standard deviation, and rms) are computed from the difference between the "truth" and estimated images for each algorithm option. The noise-only rms statistic is created by taking the square root of the difference of the squared noisy and noise-free rms values. DIB images are created by collecting and averaging all measurements whose center falls within each base pixel size grid element. For comparison with high-resolution BG and rSIR images. in this paper, the DIB image is pixel-replicated to match the pixels of the rSIR or BG images.

Fig. 5 illustrates a typical simulation result for the dual pass case. It shows the true image and the noisy image estimates. The error statistics for this case are given in Table III. For this example, the image size is 448 × 224 pixels with $P_s =$ 3.125-km-sized pixels. For most cases, the error is effectively zero mean. For all cases, multiple passes have the smallest error. The rms error is the smallest for the rSIR results, followed by BG. Visually, DIB and AVE are similar, while rSIR images better define edges. The spots are much more visible in the rSIR and BG images than in the DIB images, though the rSIR and BG images have a higher apparent noise "texture." The BG image resembles the rSIR image but is noisier.

TABLE IV

rSIR SIMULATION ERROR STATISTICS VERSUS PIXEL GRID SIZE FOR TWO PASSES AND 20 ITERATIONS

Grid	Size	Mean	STD	RMS
CETB	1.526 km	0.04	5.14	5.14
CETB	3.125 km	0.01	5.16	5.16
CETB	6.25 km	0.02	5.12	5.12
CETB	12.5 km	0.01	3.93	3.93
CETB	25 km	0.03	3.00	3.00
SMAP	1.5 km	0.01	5.12	5.12
SMAP	3 km	0.02	5.14	5.14
SMAP*	6 km	0.01	5.31	5.31
SMAP	9 km	0.02	4.27	4.27
SMAP*	12 km	0.03	3.95	3.95
SMAP	18 km	0.01	3.61	3.61

* Extended

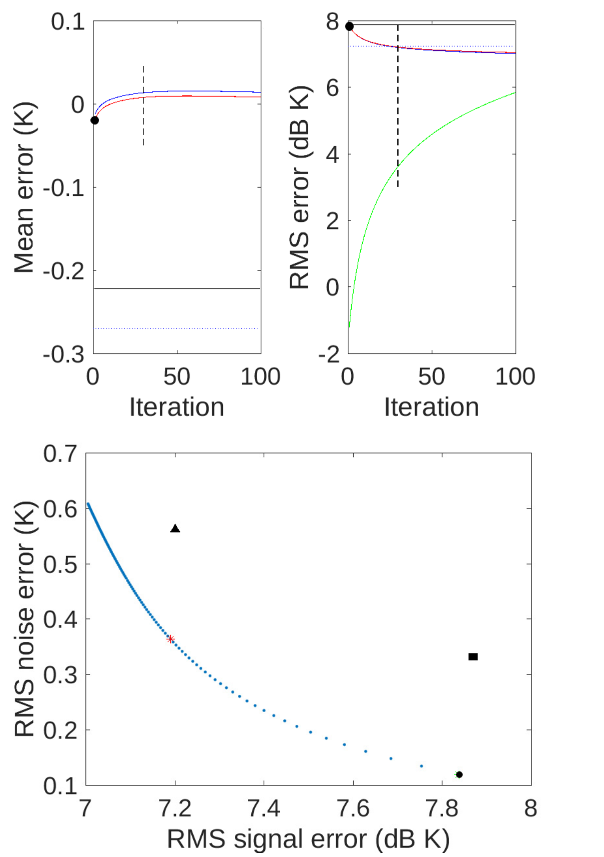

Fig. 8. (Top) rSIR error versus iteration number. (Top left) Mean error. (Top right) RMS error. Red line: noisy measurement case. Blue line: noise-free measurement case. Green is the noise power computed from the difference between the noisy and noise-free cases. Green line: vertically displaced for clarity. The large spot is the error for the AVE image. The "optimum" (minimum error) number of iterations occurs at the minimum of the red curve. For reference, the vertical dashed line is shown at 20 iterations. The horizontal dotted line shows the optimum (minimum) BG value, while the solid line is the DIB value. (Bottom) RMS noise power versus rms signal error for each iteration, which extends from right to left. Large square: DIB result. Large black dot: AVE. Red star: rSIR at 20 iterations. Triangle: BG at its optimum γ. Note that rSIR has similar signal error BG but less noise.

A. Selection of Pixel Size

DIB images are formed at the base pixel size for each projection (see Tables I and II)). A key question in applying

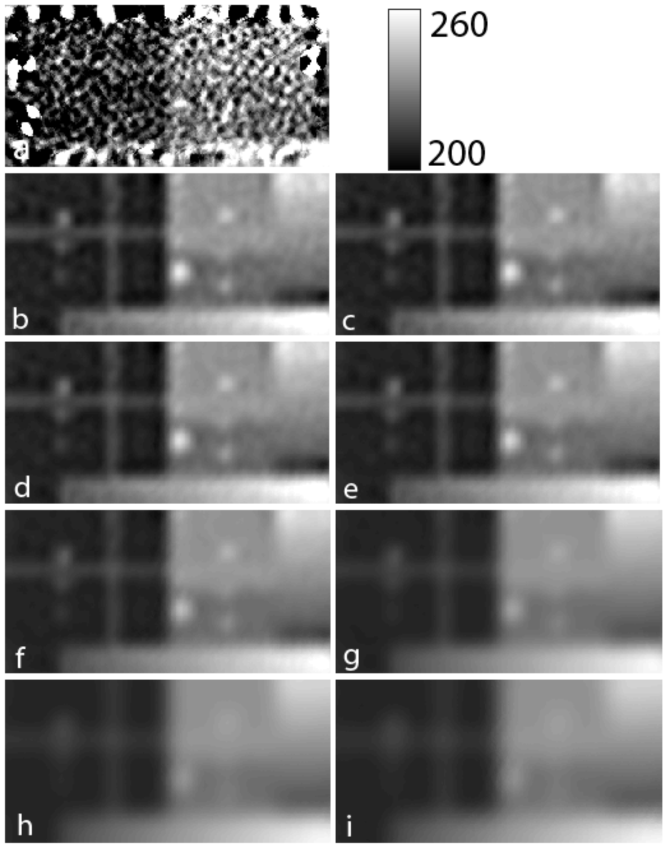

Fig. 9. BG simulation images for various values of γ'. (a) $\gamma' = 0$, rms error = 90 K. (b) $\gamma' = 0.15$, rms error = 7.26 K. (c) $\gamma' = 0.2$, rms error = 6.62 K. (d) $\gamma' = 0.25$, rms error = 6.22 K. (e) $\gamma' = 0.325$, rms error = 5.84 K. (f) $\gamma' = 0.425$, rms error = 5.49 K. (g) $\gamma' = 0.475$, rms error = 5.29 K. (h) $\gamma' = 0.495$, rms error = 5.53 K. (i) $\gamma' = 0.5$, rms error = 6.35 K. The true image is shown in Fig. 5(a).

reconstruction processing is determining the appropriate fine pixel resolution. The problem is simplified by the small number of "standard" pixel sizes available for each projection family (see Tables I and II).

Table IV compares the simulation error versus pixel size for both CETB and SMAP standard grids. Comparing similar pixel sizes from the different projections suggests that the projection choice has only a very limited effect—the pixel size is the most critical factor, and there is a tradeoff between pixel size and noise level. Since the computation increases with decreasing pixel size, larger pixel sizes are generally preferred to minimize the computational load. However, finer pixels are desired to exploit the finer resolution possible with the reconstruction. For CETB, another consideration is compatibility with the grid sizes used by other sensor products. Thus, for CETB, we adopt the 3.125-km processing grid. Noting that the error is smaller for 3-km grid elements than for 6-km elements, we adopt the 3-km grid size for the SMAP grid product.

B. Selecting the rSIR Number of Iterations

As noted in [2], there is a tradeoff between the reconstruction accuracy and the noise level. Truncating the rSIR iteration at an appropriate point minimizes the overall error.

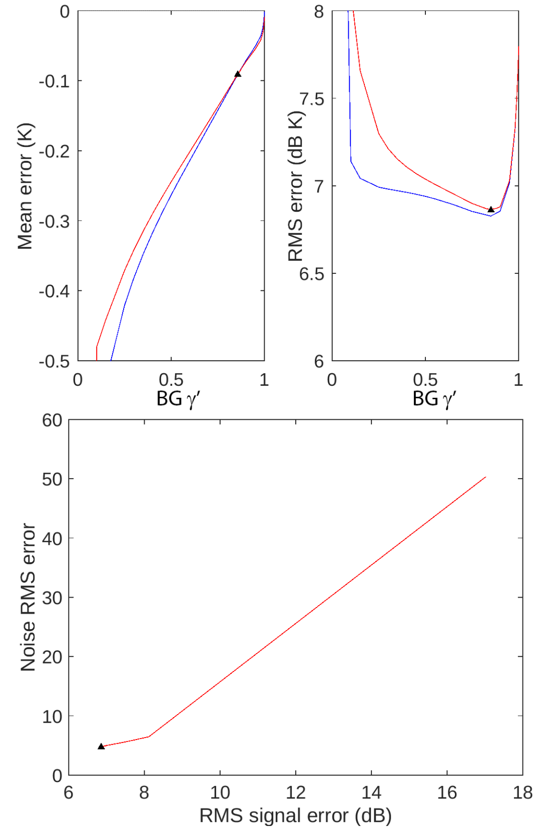

Fig. 10. (Top) BG error versus γ'. (Top left) Mean error. (Top right) RMS error. The locations of the optimum (i.e., the minimum rms error) values are indicated with black triangles. Red line: noisy BG. Blue line: median-filtered case. (Bottom) RMS noise versus rms signal error for different γ'. These lines coincide in the plot.

TABLE V

SQUARE ROOT OF MEASURED SRF AREA (IN KILOMETERS) AT VARIOUS CUTOFF LEVELS

Case	-3 dB	-10 dB	-20DB
AVE	61.4	106.9	137.5
DIB	51.35	88.7	112.8
BG	44.3	70.8	81.5
rSIR	46.9	74.7	106.6

To understand the tradeoff between the number of iterations and signal and noise, Fig. 8 plots the mean, standard deviation, and rms error versus iteration. Also shown in this figure are the errors for the DIB and AVE (the first iteration of rSIR) images. As the number of iterations is increased, the images sharpen and the details become more evident, which is reflected in the fact that the signal rms error decreases; however, the noise level also increases with increasing iteration. Thus, while the iteration improves the signal, excessive iteration can overly enhance the noise. Noting that we can stop the rSIR iteration at any point, we somewhat arbitrarily choose a value of 20 iterations, which provides good signal performance and only slightly degraded the noise performance. This is the value used in Table III, where we see that the overall error performance of the rSIR reconstruction is better than the DIB and BG results.

To understand the effects of grid size, the simulations were repeated for different values of N_s and different number of

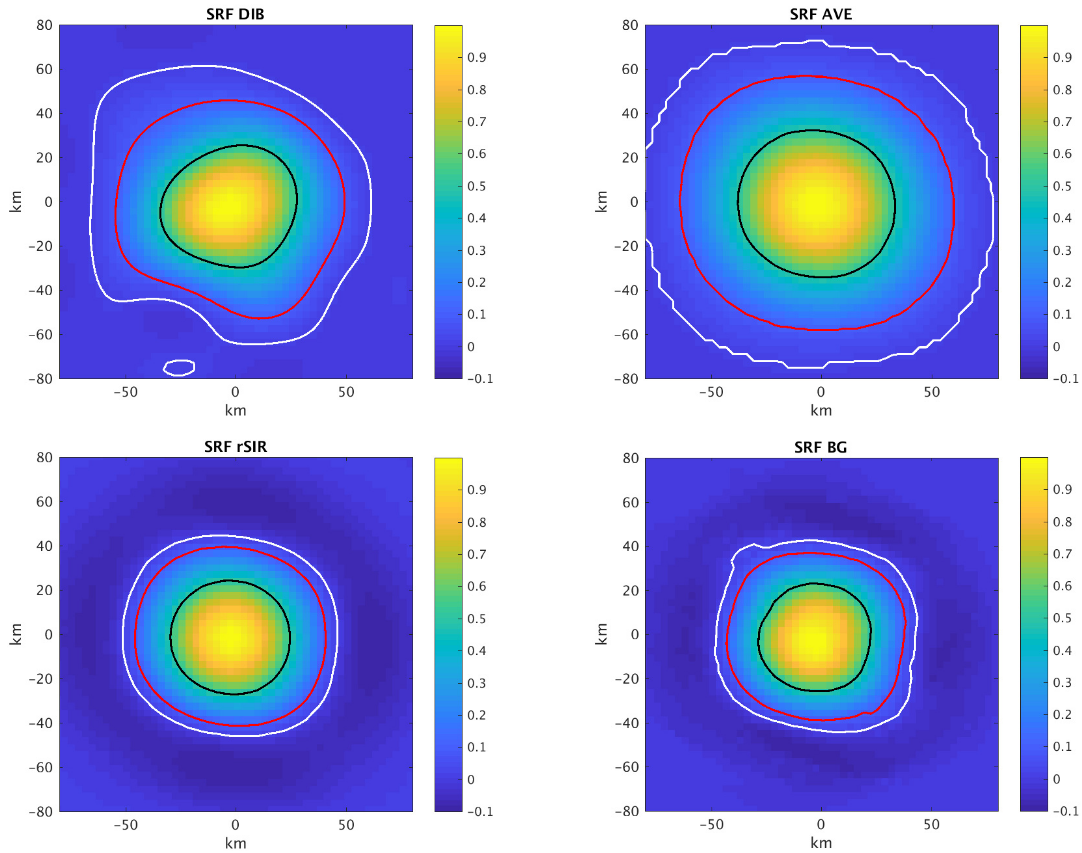

Fig. 11. Representative estimated MRFs for (Top left) DIB, (Top right) AVE, (Bottom left) rSIR, and (Bottom right) BG. Black contours are at −3 dB, the red contour are at −6 dB, and the white contours are at −10 dB from the normalized peak at the center. Note that rSIR and BG both have smaller −3- and −6-dB contours than AVE, with rSIR slightly smaller than BG.

passes. Although the numerical values of the rms error change, the overall ranking and relative spacing of the DIB, rSIR, and BG values are the same for all cases. Detailed analysis of each comparison is not presented, but the results can be summarized as follows.

1) Within a wide range of the number of iterations employed, the error and resolution performance of rSIR is better than DIB. rSIR provides better effective resolution than DIB.
2) Based on the rms error comparison, the performance of rSIR is slightly better than BG with the optimum γ, and thus rSIR is preferred over BG.

These observations are consistent with those from other satellite radiometers considered in the CETB [2].

C. Selecting the Optimum BG γ

As previously noted, the BG approach requires selection of a subjective tuning parameter γ, which controls the regularization and relative weighting between signal reconstruction and noise enhancement. The value of γ can range from 0 to $\pi/2$. Note that, for simplicity, in the captions and plots, the symbol γ' or g are sometimes used, which are related to γ by $\gamma = (\pi/2)\gamma'$ and $\gamma = \pi g$. Fig. 9 compares the images resulting from different γ' values. Note that as γ is varied between its extremes, the images vary from smooth but not very detailed, to having greater detail, but also excessive noise and artifacts. As seen in Fig. 5, at value of γ corresponding

TABLE VI

INVERSE RADIUS OF THE SRF SPECTRUM AREA EXPRESSED (IN KILOMETERS) AT VARIOUS CUTOFF LEVELS. SMALLER VALUES CORRESPOND TO FINER RESOLUTION

Case	-3 dB	-10 dB	-20DB
AVE	63.1	37.1	26.9
DIB	52.2	30.7	22.0
BG	30.7	22.6	18.8
rSIR	30.0	23.7	20.4

to the minimum total error ($\gamma' = 0.425$), the rSIR and BG results appear similar, though rSIR has slightly better error performance (see Table III).

Note that due to the occasional poorly conditioned matrix, some BG-estimated pixels have extreme values. These can be suppressed by applying a 3×3 median filter after the BG processing. The median filter reduces the rms error in the image. The median filter is edge preserving and so has minimal effect on the image quality.

For small values of γ', the noise is the most enhanced but the features are the sharpest. For larger values of γ', the noise texturing is reduced but features are smoothed. A plot of the rms error versus γ' is shown in Fig. 10. We note that BG requires significantly more computation than does rSIR since it requires creating and inverting a matrix for each image pixel. This makes using BG very difficult for large images, and is a factor in the selection of rSIR for use in the CETB.

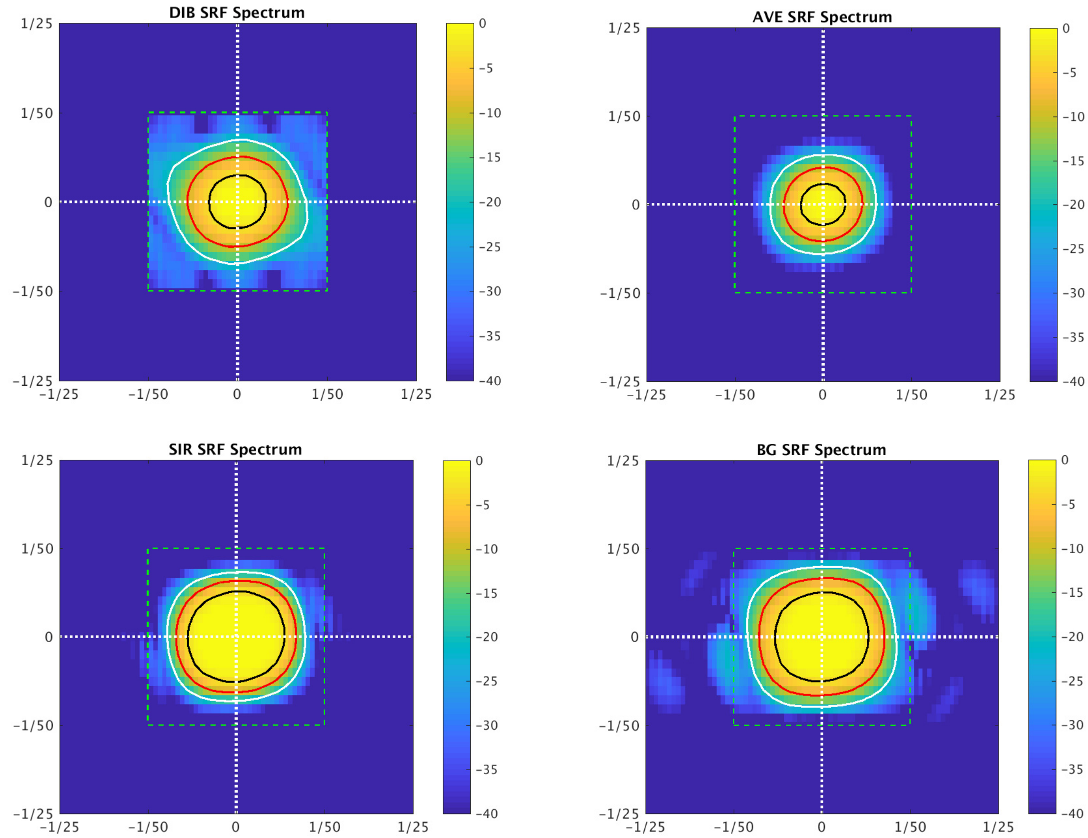

Fig. 12. Spectrum of MRFs for (Top left) DIB, (Top right) AVE, (Bottom left) rSIR, and (Bottom right) BG. Black contours are at −3 dB, the red contours are at −6 dB, and the white contours are at −10 dB from the normalized peak at the center. The green dashed square is at a spatial frequency of 1/50 km^{-1}. Note that rSIR and BG have wider frequency responses, and therefore finder resolution than DIB and AVE. rSIR and BG have similar −3-dB responses, but rSIR has a faster rolloff at higher frequencies and, thus, is less sensitive to noise.

V. Pixel Response Functions

The MRF describes the spatial characteristics of an *individual measurement* while the pixel SRF describes the spatial characteristics of the estimated *pixel*. In effect, the SRF is the impulse response of the measurement system, including the reconstruction. Analysis of the SRF validates the effective resolution of the image reconstruction.

In AVE, DIB, and BG, the pixel value is the weighted linear sum of measurements included in the pixel value. Thus, the SRF can be computed as the weighted sum of the measurement MRFs. Note that the SRF can vary from pixel to pixel due to the differences in location of the measurement within the pixel area and variations in the MRFs for the measurements. (This variation in the MRF precludes the use of deconvolution algorithms.) To compute the approximate SRF of rSIR, we use a simulation of a synthetic truth image consisting of a delta function, i.e., a single large-valued pixel, with other pixel values set to the background value [13]. The result is normalized to 1. The effective resolution can be evaluated as the area of the SRF greater than a particular threshold. These values are tabulated in Table V. Note that while rSIR and BG are similar, by this metric, BG provides somewhat finer resolution.

Another measure of the effective resolution of the SRF is obtained by considering the spectrum of the SRF. For this, we compute the Fourier transforms of the SRFs in Fig. 11, shown in Fig. 12. As a measure of the spectral resolution, the area in spatial frequency units is computed. This is converted into an equivalent circular radius (the resolution) by scaling the area by $1/\pi$. The inverse of this value is shown for each case in Table VI. By this measure, rSIR provides the finest resolution for the −3-dB contour level, with BG providing somewhat greater frequency content at the −20- and −10-dB levels. We note that the faster rolloff of rSIR helps explain why it has lower noise than BG.

VI. Actual Data

Having selected the grid size and regularization parameters based on simulation, in this section, we compare the performance of DIB and rSIR image reconstruction applied to actual data (see Fig. 13). These evening ltod images are small (250 km × 250 km) subimages extracted from the full EASE-Grid 2.0 Northern Hemisphere grid using the selected grid size and algorithm parameters derived from simulation. Lacking T_B ground-truth data, T_B errors cannot be directly computed. A visual comparison of the images reveals improved detail in the rSIR and BG images compared to the DIB images. As expected, the DIB images are blocky, while the high-resolution images exhibit finer resolution. Subjectively, the rSIR images have the highest contrast and appear more detailed than the BG images. The BG images exhibit greater texturing and noise compared to the rSIR images.

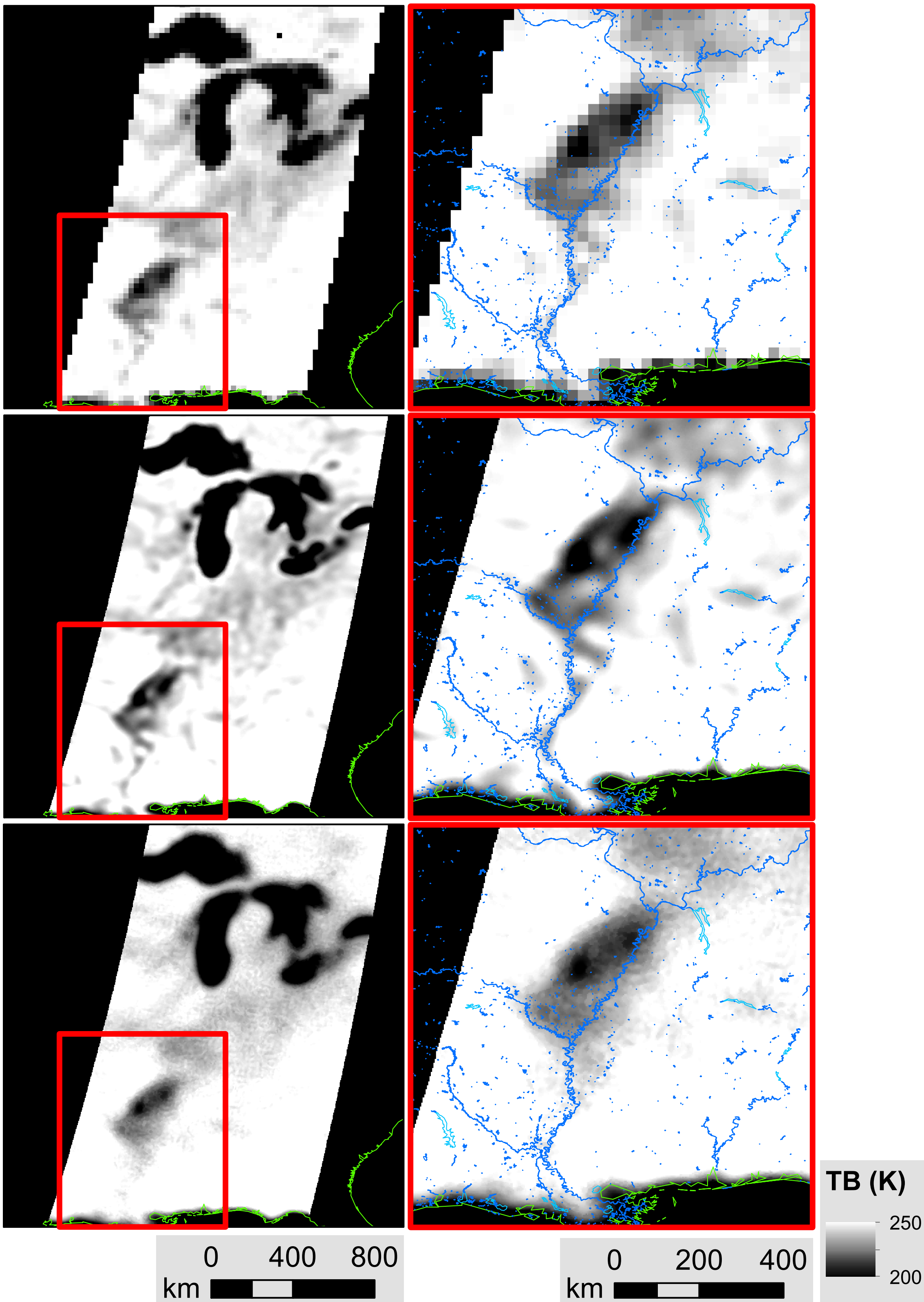

Fig. 13. Northern Hemisphere SMAP Radiometer EASE-Grid 2.0 1.4 GHz, vertically polarized, brightness temperature images, single morning overpasses, day of year 092, 2015, demonstrating spatial resolution enhancement from (Top row) 25-km DIB to(Center row) 3.125-km rSIR, and(Bottom row) 3.125-km BG. The left column shows the U.S. Midwest Mississippi Valley, from the Great Lakes to the Gulf of Mexico, with (green) Global Self-Consistent, Hierarchical, High-Resolution Geography Database coastlines [22]. The right column is magnified area of respective DIB, rSIR, and BG images, with (blue) Global Lakes and Wetlands Database Level 2 rivers and wetlands [23]. Note colder brightness temperature area evident along Mississippi Valley, with greater detail in rSIR and BG image reconstructions.

In these images, the cooler (darker) areas generally correspond to regions with greater soil moisture. The dark patch west of the Mississippi River is the result of intense rain in the preceding days before these data are collected. However, we note that derived soil moisture estimates include other factors such as soil type and vegetation cover, which is not directly evident in the T_B images. In later papers, we use the derived T_B images to compare derived soil moisture with *in situ* soil moisture measurements.

VII. Conclusion

This paper focuses on the production of stand-alone SMAP T_B image products at enhanced resolution. These can be directly used in vegetation and land studies or as input to SMAP soil moisture estimation algorithms to generate high-resolution soil moisture maps. The SMAP T_B images will be incorporated into the NASA-sponsored CETB ESDR, which includes a long time series of consistently calibrated T_B images from SMMR, SSM/I, SSMIS, and AMSR-E [1], and will be employed in generating high-resolution soil moisture maps.

This paper has compared the performance of the rSIR, BG, and DIB image production methods. The effects of grid size selection have been considered, and the tradeoffs in selecting the values of the regularization parameters in BG and rSIR are considered. The results demonstrate that reconstruction using rSIR and BG produce a finer resolution, lower rms errors images than DIB. The rSIR and BG algorithms produce similar, though not identical, results, with rSIR exhibiting slightly lower noise based on simulation. rSIR has a finer resolution by some metrics. Because rSIR requires significantly less computation, rSIR is adopted for generating SMAP enhanced resolution for CETB.

References

[1] M. J. Brodzik and D. G. Long. (2018). *Calibrated Passive Microwave Daily EASE-Grid 2.0 Brightness Temperature ESDR (CETB): Algorithm Theoretical Basis Document, National Snow and Ice Data Center (NSIDC) Publication*. [Online]. Available: http://nsidc.org/pmesdr/files/MEaSUREs_CETB_ATBD_v1.0.pdf

[2] D. G. Long and M. J. Brodzik, "Optimum image formation for space-borne microwave radiometer products," *IEEE Trans. Geosci. Remote Sens.*, vol. 54, no. 5, pp. 2763–2779, May 2016, doi: 10.1109/TGRS.2015.2505677.

[3] J. Piepmeier, P. Mohammed, G. De Amici, E. Kim, J. Pen, and C. Ruf. (Dec. 10, 2014). *Algorithm Theoretical Basis Document (ATBD) SMAP Calibrated, Time-ordered Brightness Temperatures L1B_TB Data Product*. [Online]. Available: https://smap.jpl.nasa.gov/system/internal_resources/details/original/278_L1B_TB_RevA_web.pdf

[4] M. J. Brodzik, B. Billingsley, T. Haran, B. Raup, and M. H. Savoie, "EASE-Grid 2.0: Incremental but significant improvements for earth-gridded data sets," *ISPRS Int. J. Geo-Inf.*, vol. 1, no. 1, pp. 32–45, 2012.

[5] M. J. Brodzik, B. Billingsley, T. Haran, R. Raup, and M. H. Savoie, "EASE-Grid 2.0: Incremental but significant improvements for Earth-gridded data sets," *ISPRS Int. J. Geo-Inf.*, vol. 3, no. 3, pp. 1154–1156, 2014.

[6] G. E. Backus and J. F. Gilbert, "Numerical applications of a formalism for geophysical inverse problems," *Geophys. J. Roy. Astron. Soc.*, vol. 13, nos. 1–3, pp. 247–276, Jul. 1967.

[7] G. E. Backus and J. F. Gilbert, "Resolving power of gross Earth data," *Geophys. J. Roy. Astron. Soc.*, vol. 16, pp. 169–205, Oct. 1968.

[8] A. Stogryn, "Estimates of brightness temperatures from scanning radiometer data," *IEEE Trans. Antennas Propag.*, vol. AP-26, no. 5, pp. 720–726, Sep. 1978.

[9] D. G. Long and D. L. Daum, "Spatial resolution enhancement of SSM/I data," *IEEE Trans. Geosci. Remote Sens.*, vol. 36, no. 2, pp. 407–417, Mar. 1998.

[10] D. S. Early and D. G. Long, "Image reconstruction and enhanced resolution imaging from irregular samples," *IEEE Trans. Geosci. Remote Sens.*, vol. 39, no. 2, pp. 291–302, Feb. 2001.

[11] F. T. Ulaby and D. G. Long, *Microwave Radar and Radiometric Remote Sensing*. Ann Arbor, MI, USA: University of Michigan Press, 2014.

[12] J. Chaubell *et al.*, "Backus-Gilbert optimal interpoaltion applied to enhance SMAP data: Implementation and assessment," in *Proc. IEEE Int. Geosci. Remote Sens. Symp. (IGARSS)*, Jul. 2017, pp. 2531–2534, doi: 10.1109/IGARSS.2017.8127510.

[13] D. G. Long, "Comparison of SeaWinds backscatter imaging algorithms," *IEEE J. Sel. Topics Appl. Earth Observ. Remote Sens.*, vol. 10, no. 5, pp. 2214–2231, May 2017, doi: 10.1109/JSTARS.2016.2626966.

[14] H. G. Feichtinger and K. Gröchenig, "Iterative reconstruction of multivariate band-limited functions from irregular sampling values," *SIAM J. Math. Anal.*, vol. 23, no. 1, pp. 244–261, 1992.

[15] K. Gröchenig, "Reconstruction algorithms in irregular sampling," *Math. Comput.*, vol. 59, no. 199, pp. 181–194, 1992.

[16] D. G. Long and R. O. W. Franz, "Band-limited signal reconstruction from irregular samples with variable apertures," *IEEE Trans. Geosci. Remote Sens.*, vol. 54, no. 4, pp. 2424–2436, Apr. 2016.

[17] B. Caccin, C. Roberti, P. Russo, and L. A. Smaldone, "The Backus–Gilbert inversion method and the processing of sampled data," *IEEE Trans. Signal Process.*, vol. 40, no. 11, pp. 2823–2825, Nov. 1992.

[18] A. N. Tikhonov and V. Y. Arsenin, *Solutions of Ill-posed Problems*. Washington, WA, USA: Winston & Sons, 1977.

[19] W. D. Robinson, C. Kummerow, and W. S. Olson, "A technique for enhancing and matching the resolution of microwave measurements from the SSM/I instrument," *IEEE Trans. Geosci. Remote Sens.*, vol. 30, no. 3, pp. 419–429, May 1992.

[20] M. R. Farrar and E. A. Smith, "Spatial resolution enhancement of terrestrial features using deconvolved SSM/I microwave brightness temperatures," *IEEE Trans. Geosci. Remote Sens.*, vol. 30, no. 2, pp. 349–355, Mar. 1992.

[21] P. Chakraborty, A. Misra, T. Misra, and S. S. Rana, "Brightness temperature reconstruction using BGI," *IEEE Trans. Geosci. Remote Sens.*, vol. 46, no. 6, pp. 1768–1773, Jun. 2008.

[22] P. Wessel and W. H. F. Smith. (2015). *A Global Self-consistent, Hierarchical, High-resolution Geography Database Version 2.3.7*. Digital Media. [Online]. Available: http://www.soest.hawaii.edu/pwessel/gshhg

[23] B. Lehner and P. Döll, "Development and validation of a global database of lakes, reservoirs and wetlands," *J. Hydrol.*, vol. 296, nos. 1–4, pp. 1–22, 2004.

David G. Long (S'80–SM'98–F'08) received the Ph.D. degree electrical engineering from the University of Southern California, Los Angeles, CA, USA, in 1989.

From 1983 to 1990, he was with the NASA's Jet Propulsion Laboratory (JPL), Pasadena, CA, USA, where he was involved in the development of advanced radar remote sensing systems. While at JPL, he was the Project Engineer on the NASA Scatterometer (NSCAT) Project which flew from 1996 to 1997. He also managed the SCANSCAT Project, the precursor to SeaWinds which was flown in 1999 on QuikSCAT, in 2002 on ADEOS-II, and in 2014 on the International Space Station. He is currently a Professor with the Electrical and Computer Engineering Department, Brigham Young University (BYU), Provo, UT, USA, where he teaches upper division and graduate courses in communications, microwave remote sensing, radar, and signal processing, and also the Director of the BYU Center for Remote Sensing. He is the Principal Investigator on several NASA-sponsored research projects in remote sensing. He has authored or co-authored more than 400 publications in various areas including signal processing, radar scatterometry, and synthetic aperture radar. His research interests include microwave remote sensing, radar theory, space-based sensing, estimation theory, signal processing, and mesoscale atmospheric dynamics.

Dr. Long received the NASA Certificate of Recognition several times. He is an Associate Editor of IEEE Geoscience and Remote Sensing Letters.

Mary J. Brodzik received the B.A. degree *(summa cum laude)* in mathematics from Fordham University, Bronx, NY, USA, in 1987.

Since 1993, she has been with the National Snow & Ice Data Center (NSIDC), Cooperative Institute for Research in Environmental Sciences (CIRES), University of Colorado Boulder, Boulder, CO, USA, where she implemented software systems to design, produce, and analyze snow and ice data products from satellite-based visible and passive microwave imagery. She has contributed to the NSIDC data management and software development teams for the NASA Cold Lands Processes Experiment and Operation IceBridge. She is a Principal Investigator of the NASA Making Earth Science Data Records for Use in Research Environments Calibrated Enhanced-Resolution Brightness Temperature Project, where she is managing the operational production of a 37-year EASE-Grid 2.0 Earth Science Data Record of satellite passive microwave data. She is using MODIS data products to derive the first systematically derived global map of the world's glaciers. Under a grant from the U.S. Agency for International Development, she is developing snow and glacier ice melt models to better understand the contribution of glacier ice melt to major rivers with headwaters in High Asia. She is currently a Senior Associate Scientist with the NSIDC, CIRES, University of Colorado Boulder. She was involved in software development, validation, and verification on the Defense Department satellite command and control and satellite tracking systems. Her research interests include optical and passive microwave sensing of snow, remote sensing data gridding schemes, and effective ways to visualize science data.

Molly A. Hardman received the B.Sc. degree (Hons.) in physics from the University of KwaZulu-Natal, Durban, South Africa, in 1976, and the M.S. degree in aerospace engineering from the University of Colorado at Boulder, Boulder, CO, USA, in 1991.

She was with the National Snow and Ice Data Center (NSIDC), University of Colorado at Boulder, from 1989 to 1993, and returned to work at the Center in 2013. In the intervening years, she worked in scientific software development, including on software that flew on the final mission of the Space Shuttle Columbia. She also owned and operated her own company manufacturing and selling high powered HF amplifiers. She is currently a Senior Associate Scientist with the NSIDC, Cooperative Institute for Research in Environmental Sciences, University of Colorado at Boulder, where she works on software to process and analyze passive microwave data.